Int. J. Heat Mass Transfer. Vol. 29, No. 3, pp. 475–485, 1986
Printed in Great Britain

0017–9310/86 $3.00 + 0.00

Three-dimensional natural convection heat transfer of a liquid metal in a cavity

R. VISKANTA, D. M. KIM and C. GAU
Heat Transfer Laboratory, School of Mechanical Engineering, Purdue University, West Lafayette, IN 47907, U.S.A.

(*Received* 19 *July* 1985 *and in final form* 23 *October* 1985)

Abstract—The paper describes a numerical algorithm for the solution of the steady-state Navier–Stokes equations in three dimensions for the problem of natural convection in a rectangular cavity as a result of differential side heating. Numerical results for two- and three-dimensional models are reported for a cavity filled with a low-Prandtl-number fluid. Supporting experiments using gallium as a working fluid are described. Measured temperatures are compared with predictions of the three-dimensional model. Agreement between data and predictions is only fair and reasons for the discrepancy are identified.

1. INTRODUCTION

THERE has been considerable recent interest in thermally driven flows in rectangular cavities in which the heating is imposed differentially on the two end walls [1–3]. For any small, non-zero temperature contrast there will be generally unicellular motion up the hot wall, across the top of the cavity, down the cold wall, and returning across the bottom. The applications range from geophysical processes to single-crystal growth from melts. The state of the art has been recently reviewed, important critical issues discussed and future research needs identified [4]. This paper is concerned with three-dimensional natural convection in a liquid metal filled cavity. There are two questions needing attention: three-dimensional vs two-dimensional effects in finite-size enclosures and the need of experimental data for liquid metals. Natural convection in rectangular cavities filled with a low-Prandtl-number liquid in which heating or cooling is imposed differentially on the two end walls is of practical interest to a number of important applications such as solidification of castings, purification of materials, growth of single crystals from melts, and many others.

Extensive review of experimental work on natural convection in enclosures has failed to reveal significant dependence of the Nusselt number on the Prandtl number for a Prandtl number greater than 0.7 and a fixed Rayleigh number [5]. However, low-Prandtl-number fluids (liquid metals, semiconductors) are expected to act differently to high-Prandtl-number fluids because fluid inertia plays a much more important role in the convective process. Some work has been done on predicting natural convection flow and heat transfer in three-dimensional enclosures filled with ordinary fluids [6–10]. For example, three-dimensional natural convection of ordinary fluids in horizontal, rectangular cavities of several different aspect ratios has been studied [7]. The conclusions of ref. [7] were that the overall heat transfer is determined by the entire three-dimensional flow field and further that the correct flow configurations within a box cannot be obtained two-dimensionally. Similar conclusions have been drawn by other investigators for the even more complicated configuration of a box heated differentially and inclined at an angle with respect to the gravitational field [6, 10].

It is has been pointed out that there are few predictions and even fewer experiments were natural convection in enclosures has been studied [4]. In addition, the question of two-dimensional vs three-dimensional modeling of natural convection in enclosures has not been adequately addressed, and the conditions for which two-dimensional models are valid have not been established. The lack of results for low-Prandtl-number fluids has provided the motivation for the work reported in this paper. Two-dimensional and three-dimensional natural convection in a cavity filled with a low *Pr* fluid has been modeled numerically, and experiments have been performed to measure the temperature distribution of a liquid metal in the enclosure.

2. ANALYSIS

2.1. *Physical and mathematical model*

We consider the steady, three-dimensional flow of a Boussinesq liquid in the geometry shown in Fig. 1. The enclosure is of a rectangular cross-section, with isothermal hot and cold vertical end walls. The top,

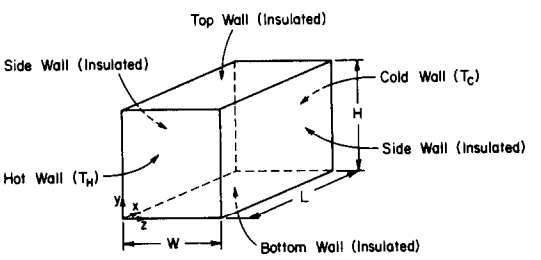

FIG. 1. Schematic diagram of the enclosure and coordinate system.

NOMENCLATURE

A_x aspect ratio of enclosure, L/H, see Fig. 1
A_z aspect ratio of enclosure, W/H, see Fig. 1
H height of enclosure, see Fig. 1
L length of enclosure, see Fig. 1
$Nu(y,z)$ local Nusselt number at hot wall, $-\partial\theta/\partial\xi|_{\xi=0}$
$\overline{Nu}(z)$ local Nusselt number (averaged over y-direction) at hot wall
$\overline{Nu}$ average Nusselt number at hot wall
P pressure
P^* dimensionless pressure, $PH/\rho U_0^2$
Pr Prandtl number, ν/α
Ra Rayleigh number, $g\beta(T_H - T_C)H^3/\alpha\nu$
S_ϕ source term
T temperature
U dimensionless velocity in the x-direction, u/U_0
U_0 reference velocity, α/H
u fluid velocity in the x-direction
V dimensionless fluid velocity in the y-direction, v/U_0
$\mathbf{V}$ velocity vector, $u\mathbf{i}+v\mathbf{j}+w\mathbf{k}$
v fluid velocity in the y-direction
W dimensionless velocity in the z-direction, w/U_0 or width of enclosure
w fluid velocity in the z-direction
x, y, z coordinates, See Fig. 1.

Greek symbols
α thermal diffusivity
β thermal expansion coefficient
η dimensionless y-coordinate, y/H
Γ diffusion coefficient
ν kinematic viscosity
ρ density
ξ dimensionless x-coordinate, x/H
ζ dimensionless z-coordinate, z/H
θ dimensionless temperature, $(T-T_C)/(T_H-T_C)$
ϕ dependent variable.

bottom and the two side walls are insulated. The flow is assumed to be laminar and three-dimensional. The fluid within is assumed to have constant properties except insofar as the buoyancy is concerned, i.e. the Boussinesq approximation of linear temperature dependence of density is utilized. The governing conservation equations of mass, momentum and energy are non-dimensionalized using scales ΔT, α/H and H, for temperature, velocity, and length, respectively. The normalized equations then become

$$\nabla\cdot\mathbf{V} = 0 \tag{1}$$

$$\mathbf{V}\cdot\nabla\mathbf{V} = Pr\nabla^2\mathbf{V} - \nabla P^* + PrRa\theta\mathbf{j} \tag{2}$$

$$\nabla\cdot(\mathbf{V}\theta) = \nabla^2\theta. \tag{3}$$

Referring to Fig. 1, the boundary conditions become

$$\theta(0,\eta,\zeta) = 1 \tag{4a}$$

$$\theta(A_x,\eta,\zeta) = 0 \tag{4b}$$

$$\theta_\eta(\xi,0,\zeta) = \theta_\eta(\xi,1,\zeta) = 0 \tag{4c}$$

$$\theta_\zeta(\xi,\eta,0) = \theta_\zeta(\xi,\eta,A_z) = 0 \tag{4d}$$

with velocity $\mathbf{V}$ equal to zero on all the boundaries. Thus, we are considering rigid impermeable walls, conducting on the ends and insulated on the top, bottom and the sides.

Inspection of equations (1)–(3) reveals that they can be written in the form

$$\nabla\cdot(\mathbf{V}\phi) = \Gamma_\phi\nabla^2\phi + S_\phi \tag{5}$$

where the function ϕ stands for the dependent variable, and Γ_ϕ and S_ϕ are the diffusion coefficient and the source term corresponding to ϕ, respectively. The definitions of the variables and coefficients are summarized in Table 1.

2.2. *Method of solution*

There are numerous techniques for solving the conservation equations of mass, momentum and energy. Some of these techniques have been assessed elsewhere [11] and the SIMPLER algorithm of Patankar [12, 13] was found to be superior with respect to the rate of convergence and stability; therefore, the algorithm is used in this work. The derivation of the discretized equations for the dimensional geometry is tedious and is not given here but it follows the approach for the two-dimensional case which is described elsewhere [12, 13]. The solution seqeuence employed is the same as suggested for the two-dimensional geometry.

The tridiagonal matrix inversion algorithm (Thomas algorithm) was employed for the solution of the algebraic finite-difference equations. The convergence criterion was based on the local mass imbalance within the cavity. If the maximum local mass imbalance was

Table 1. Definitions of ϕ, Γ_ϕ and S_ϕ

Equation	ϕ	Γ_ϕ	S_ϕ
Continuity	1	0	0
x-momentum	U	Pr	$-\partial P^*/\partial\xi$
y-momentum	V	Pr	$-(\partial P^*/\partial\eta) + PrRa\theta$
z-momentum	W	Pr	$-\partial P^*/\partial\zeta$
Energy	θ	1	0

less than 0.01% of the total mass present within the cavity, the equations were assumed to be converged.

Numerical solutions were obtained by taking advantage of the symmetry plane at $z/H = W/2$. To establish the effect of grid on the results different grids ranging from $11 \times 11 \times 6$ to $31 \times 31 \times 16$ were considered for a cubical cavity. The majority of the solutions reported in the paper were obtained with a $25 \times 25 \times 11$ mesh, which was considered to represent a reasonable compromise between accuracy and computing cost.

The mesh size limitations are felt in terms of the maximum resolution that can be achieved by a finite-difference method of solution. Velocity distributions for a cubical cavity ($Ra = 10^6$ and $Pr = 0.02$) were not too sensitive to the different grids ($15 \times 15 \times 11$, $21 \times 21 \times 11$ and $25 \times 25 \times 11$); however, the peak of the maximum velocity was shifted towards the wall as the number of mesh points was increased. The finite-difference mesh used to generate both two- and three-dimensional solutions is given with the results. The accuracy of the solutions is, of course, of considerable importance. Unfortunately, because of their demands on computer storage and time, it was not practical to explore the effects on the truncation errors of further mesh refinement in the three-dimensional solutions.

3. EXPERIMENTS

3.1. *Apparatus and instrumentation*

Steady-state natural convection experiments were performed in a rectangular test cell (Fig. 2) whose inside dimensions could be adjusted such that two different aspect ratio cavities ($A_x = 1.0$ and $A_x = 2.0$) could be obtained. The inside dimensions of one of the test cells were 6.35 cm in length, 3.81 cm in width and 6.35 cm in height, and of the second they were 8.88 cm in length, 3.81 cm in width and 4.44 cm in height. The two end walls, which served as the heat source/sink, were made of a multipass heat exchanger machined from a copper plate. The copper surfaces were plated with a 0.0127-mm-thick chromium for protection against corrosion. The top, bottom and siewalls were made of Plexiglass. The two vertical sidewalls were 1.27-cm-thick plates to support the cell; and, for better insulation, the front and back sidewalls had a 0.318 cm air gap between doule plates. One of the plates is 0.318 cm thick and the other is 0.635 cm thick. The entire test cell was insulated with styrofoam and was further wrapped with a fiber glass blanket.

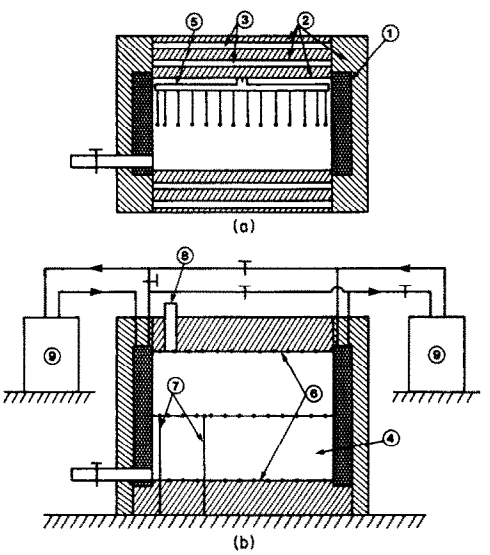

FIG. 2. Schematic diagram of the test cell, top view (a) and front view (b): (1) heat source and/or sink; (2) Plaxiglass wall; (3) air gap; (4) phase change material; (5) thermocouple rack; (6) thermocouples along the walls; (7) small diameter thermocouples; (8) hole for filling PCM; and (9) constant temperature baths.

The horizontal temperature distributions in the central region along the top wall, the center line and the bottom wall of the test cell were measured with copper–constantan (type K) thermocouples having wire diameter of 0.127 mm. A total of up to 26 (depending on A_x) equally spaced thermocouples were installed on the top and the bottom walls. The precise locations of thermocouples along the top and the bottom walls were ensured by placing them in small holes which were drilled in the walls. The thermocouples were then inserted close to the surface of the walls and were then sealed. A total of up to 17 other thermocouples, used to measure the temperature distribution along the center line, were made into a thermocouple rack. Each pair of thermocouple wires was sheathed in a 0.584-mm-diam. stainless steel tube and were then attached perpendicularly to a 2.38-mm-diam. stainless steel tube. The sheathed thermocouples were arranged in a horizontal plane and in a direction perpendicular to the front and the back walls where the temperature gradient in the liquid was the smallest (Fig. 2). The arrangement minimized heat conduction along the small stainless steel tubes and therefore reduced the measurement error.

The text cell was placed in a transparent box made of acrylic (Lexan) where the temperature could be regulated and kept constant by a temperature controller. The purpose of the controlled environment was to reduce the temperature difference between the test cell and environment, thus minimizing the heat loss/gain from the test cell to the ambient surroundings. A heat storage material was also placed in the box to minimize the frequent on-and-off-switching of the heater and to keep the inside temperature close to a constant value.

3.2. *Experimental procedure and data reduction*

The metal used in the experiments was gallium. It had a purity of 99.6% and a fusion temperature of 29.78°C. There were several reasons for selecting gallium. First, the thermophysical properties are reasonably well established [14]. Second, it has a fusion temperature close to the ambient, which is conducive for

experimentation. Third, the metal is important technologically as it is usually combined with other pure elements to form electronic and industrial materials such as semiconductors, laser diodes, solar cells, and magnetic bubble devices. The main disadavatange is that is is very expensive (about U.S. $1/g, depending on purity), and this necessitated use of a small test cell.

Before each experiment the metal was melted and poured into the preheated test cell through the sprue on the left side (Fig. 2). Provision was made to avoid air bubble entrapment in the test cell. This was accomplished during the filling procedure by slightly lifting one of the side walls where a small hole had been drilled near the top plate. This hole was sealed after the test cell was filled.

Since gallium is opaque the flow structure could not be directly observed; flow visualization experiments were performed with water. The Prandtl number of gallium is more than two orders of magnitude smaller than that of water; therefore, the flow patterns were not expected to be the same for the two fluids even though the Rayleigh numbers were identical. At best, only some qualitative understanding could be hoped for. A small amount of fish scale particles was used as a flow tracer in order to observe fluid motion. A plane sheet of laser radiation, produced by passing the beam through a cylindrical lens, was used to irradiate the fluid at different planes in the text cell. A very thin (<2 mm) velocity boundary layer was observed near the heat source and the heat sink where the velocity was relatively high. Along the horizontal top and bottom walls of the cell the horizontal fluid motion was very weak. In the core the fluid was practically stagnant. The observations are similar to the findings of others for silicone oil [15].

4. RESULTS AND DISCUSSION

4.1. *Flow structure*

The effects of Rayleigh and Prandtl numbers as well as cavity geometry on the flow structure for ordinary fluids has been discussed in the literature [7]; therefore, only one representative solution is presented for a cubical cavity with $Ra = 10^6$ and $Pr = 0.02$. As a reference, results for natural convection of ordinary fluids in two-dimensional square cavities have also been reported [7, 16]. Quantitative presentation and display of three-dimensional flow field results is difficult; therefore, the results for different velocity components are given in terms of velocities at different planes.

The horizontal (U) and vertical (V) velocity components in the x–y-plane are given in Figs. 3 and 4, respectively. The dimensionless velocity scale is indicated directly on each panel of the figures. For example, in Figs. 3(a) and 3(b) the U-velocity distributions are given at five different locations at $x/H = 0.125$, 0.300, 0.475, 0.650 and 0.875. A similar type of presentation of results is given for other planes.

As expected, at the bottom of the cavity the axial flow is directed towards the hot wall at $x/H = 0$ and at the top of the cavity the axial flow is directed towards the cold wall at $x/H = 1.0$ [Figs. 3(a) and 3(b)]. In contrast to ordinary fluids [7, 16], the boundary layers at the top and bottom walls are quite thick and extend to about the center of the cavity. Comparison of panels (a) and (b) of Fig. 3 reveals the axial velocities in the plane x–y through $z/H = 1/4$ are smaller than those through the plane at $z/H = 1/2$. The flow in the axial (x-direction) is stronger than the vertical (y-direction) and is not confined to the boundary layers (compare Figs. 3 and 4), and the boundary layers along the hot and cold end walls are seen to be thinner than along the horizontal walls. Figure 4 suggests that there are two weak counter-rotating cells in the cavity. This is more clearly shown in Fig. 5(a) where the magnitude of the velocity vector in the axial–vertical (x–y-plane through $z/H = 1/2$) has been plotted. The arrows denote the direction and magnitude of the resolved U and V velocity components at each grid point. The results show clearly the three-dimensional and recirculating nature of flow in the cavity. The velocity vectors of Fig. 5(b) indicate that closer to the vertical sidewall (the x–y-

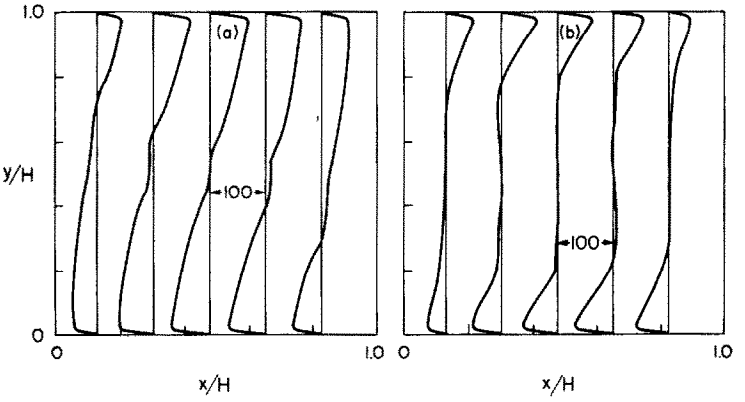

FIG. 3. Horizontal U-velocity (in the x-direction) distributions in the x–y-plane through $z/H = 1/2$ (a) and through $z/H = 1/4$ (b): $Ra = 10^6$, $Pr = 0.02$, $A_x = A_z = 1.0$.

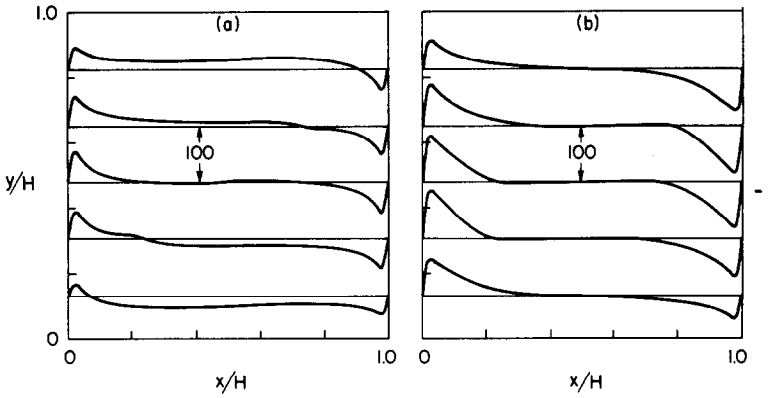

FIG. 4. Vertical V-velocity (in the y-direction) distributions in the x–y plane through $z/H = 1/2$ (a) and through $z/H = 1/4$ (b): $Ra = 10^6$, $Pr = 0.02$, $A_x = A_z = 1.0$.

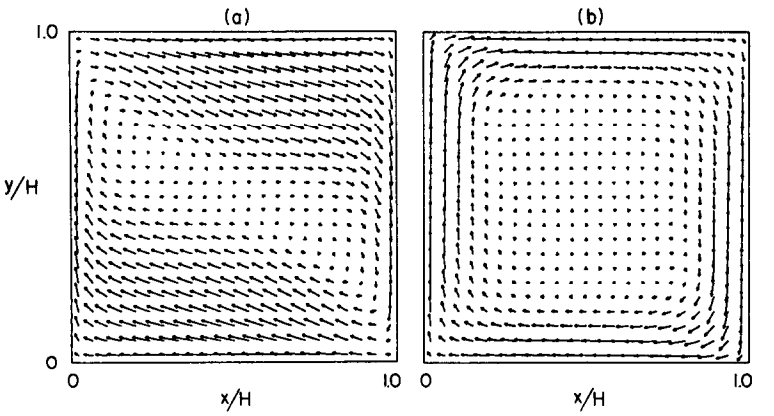

FIG. 5. Velocity vectors in the x–y-plane through $z/H = 1/2$ (a) and through $z/H = 1/4$ (b): $Ra = 10^6$, $Pr = 0.02$, $A_x = A_z = 1.0$.

plane through $z/H = 1/4$) the central core of fluid is practically stagnant.

Figures 6 and 7 depict the horizontal (x-component) and vertical (y-component) velocities in the x–z-plane, respectively. The results of Fig. 6 show that complicated multiple longitudinal flows can develop. This finding is consistent with the results of Mallinson and de Vahl Davis [7] who have concluded that such flows are a delicate function of Ra, Pr and the cavity aspect ratio. The consequences of the longitudinal flows on the local heat transfer are discussed later. Comparison of Figs. 6 and 7 shows that the maximum magnitude of the vertical velocity component is about twice as large as that of the horizontal velocity component.

4.3. *Temperature structure*

Figures 8(a) and (b) illustrate the contours of the isotherms at the midplane ($z/H = 1/2$) and at the quarter plane ($z/H = 1/4$), respectively. The dimensionless isotherms are given for a temperature difference of

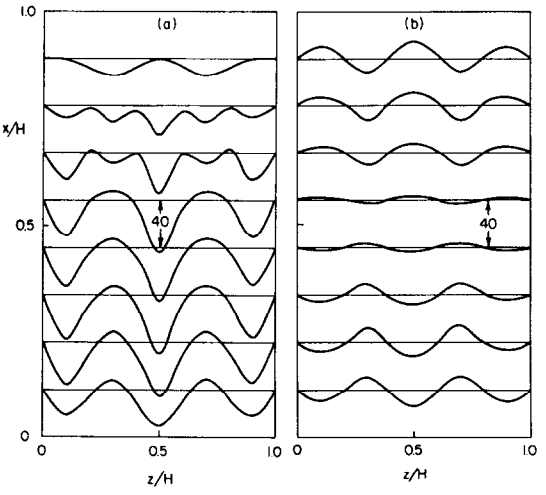

FIG. 6. Horizontal U-velocity distributions in the x–z-plane through $y/H = 1/2$ (a) and through plane at $y/H = 1/4$ (b): $Ra = 10^6$, $Pr = 0.02$, $A_x = A_z = 1.0$.

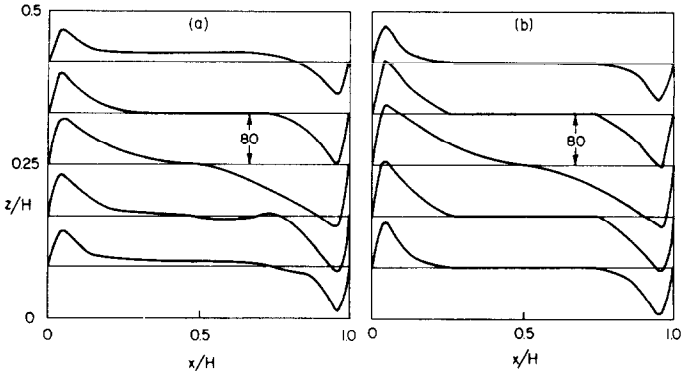

FIG. 7. Vertical V-velocity distributions in the x–z-plane through $y/H = 1/2$ (a) and through plane at $y/H = 1/4$ (b): $Ra = 10^6$, $Pr = 0.02$, $A_x = A_z = 1.0$.

$\Delta\theta = 0.1$. Vertical thermal boundary layers are clearly formed along the vertical walls. The isotherms are denser on the lower part of the hot vertical wall and on the top part of the cold vertical wall. This indicates that heat transfer through these parts of the walls is greater. The isotherms of the quarter-plane [Fig. 8(b)] are seen to be less dense than those of the midplane [Fig. 8(a)] at the lower part of the hot vertical wall, and this shows that the local heat transfer rate is larger at the midplane ($z/H = 1/2$) than the quarter-plane ($z/H = 1/4$).

The horizontal motions near the bottom and top horizontal walls carry fluid particles from one end-wall to the other and complete the circuit flow. This process produces two effects which are evident from Fig. 8. First, strong horizontal temperature gradients are maintained at the lower left and the upper right hand corners of the cavity. Second, a temperature difference is set up vertically across the interior of the cavity. Horizontal advection in the interior due to strong entrainment of fluid in and out of the boundary layers tends to make the temperature relatively uniform in the horizontal direction. Results for other Ra and Pr (not included) which were considered in this study have shown that for a given Ra the effects of Pr on the temperature distribution manifest primarily in the interior of the cavity where the effects of vertical heat diffusion is important since the temperature field in the interior of the cavity is primarily a function of z only (Fig. 8).

Panels (a) and (b) of Fig. 8 show that in the central part of the cavity $\partial\theta/\partial\xi$ is small but positive in the center of the cross-section. This is a result of the convective effect of the flow in the secondary rolls (Fig. 5). The finding is consistent with the results for ordinary fluids for sufficiently large Ra [7, 16].

For $Pr \gg 1$ the nonlinear (convection) terms in the momentum equations, equation (2), can be safely dropped, but when $Pr \ll 1$, the effect of the convection term is much more interesting. The effects of low Prandtl number manifest themselves in the interior of the cavity where, as pointed out above, vertical diffusion of heat is important. The vertical diffusion process for low-Prandtl-number fluids has not diminished because there is vertical advection in the interior to oppose it. The process becomes relatively more important as Pr decreases. Consequently, the

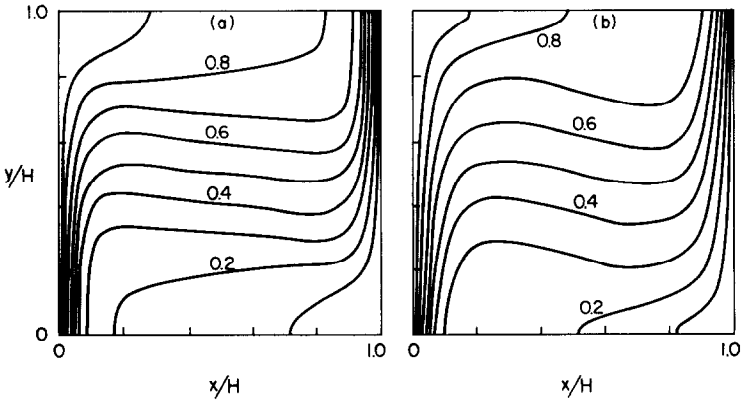

FIG. 8. Isotherms in the x–y-plane at $z/H = 1/2$ (a) and $z/H = 1/4$ (b): $Ra = 10^6$, $Pr = 0.02$, $A_x = A_z = 1.0$.

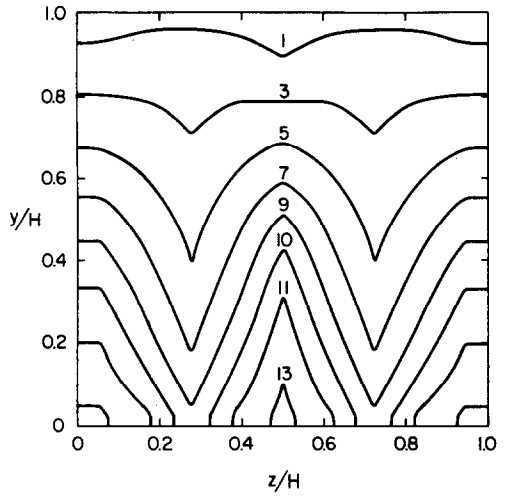

FIG. 9. Local Nusselt number [$Nu(y,z)$] contours: $Ra = 10^6$, $Pr = 0.02$, $A_x = A_z = 1.0$.

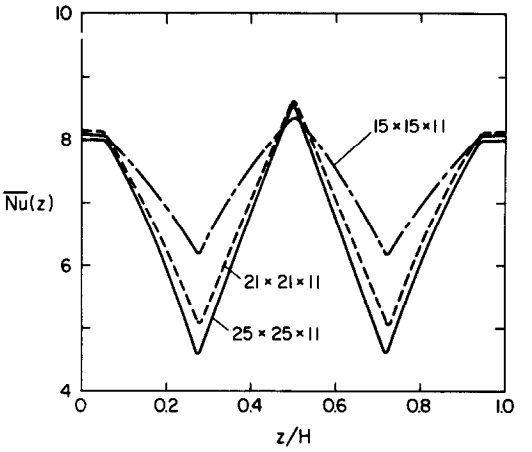

FIG. 10. Effect of grid on the local Nusselt number $\overline{Nu}(z)$ (averaged over the height of the cavity) distributions: $Ra = 10^6$, $Pr = 0.02$, $A_x = A_z = 1.0$.

vertical temperature gradient is larger and is linear over a greater vertical extent of the cavity than the higher Pr fluids [7].

4.4. *The local and average Nusselt number.*

Figure 9 shows the local Nusselt number [$Nu(y, z)$] isopleths at the hot vertical wall of the cavity. The local Nusselt number was calculated at $\xi = 0$ using a three-point approximation for $\partial\theta/\partial\xi$. The results clearly demonstrate the three-dimensional effects on local heat transfer at the hot wall. Heat transfer is maximum at lower part of the midplane ($z/H = 1/2$). This is consistent with the U-velocity distributions given in Fig. 6. The two minima to the left and to the right of the midplane correspond to the locations where there is a reversal of the U-velocity away from the hot wall.

Figure 10 shows the average Nusselt number along the z-axis. The average Nusselt number was calculated through the use of a three-point approximation of $\partial\theta/\partial\xi|_0$ and Simpson's rule to approximate

$$\overline{Nu}(\zeta) = \int_0^1 Nu(\eta, \zeta)\, d\eta. \tag{6}$$

The results are generated using three different grid sizes to assess the sensitivity of the results to the finite-difference mesh. The figure clearly shows that as the grid becomes finer, the variation of the y-direction averaged Nusselt number [see equation (6)] across the spanwise z-direction becomes greater.

The two-dimensional model equations were solved and the average Nusselt number results were compared to the three-dimensional model results in Table 2. The predictions of the two-dimensional analysis are about 10% higher than those of the three-dimensional analysis. Even though the three-dimensional effects on the local Nusselt number are apparent, the average Nusselt number calculated from a two-dimensional analysis may be used to predict heat transfer in a three-dimensional cubical cavity for a low-Prandtl-number fluid. Results for the average Nussselt number have been calculated as a function of Rayleigh number and are presented in Table 3.

The effect of the grid on the average Nusselt number is examined using two- and three-dimensional models and the results are reported in Table 2. The results of the table suggest that a grid finer than $25 \times 25 \times 11$ (= 6875 nodes) would have to be used to establish that the results are grid independent. To obtain a convergent solution with a $25 \times 25 \times 11$ mesh required about 100 iterations, and a run took 1642 s on a CYBER 205 digital computer. Vectorization of the computer program would be expected to reduce this time significantly. However, a finer grid, say, $41 \times 41 \times 21$ would still be too costly for routine three-dimensional

Table 2. Comparison of three-dimensional and two-dimensional model results for the average Nusselt number: $Ra = 10^6$, $Pr = 0.02$, $A_x = A_z = 1.0$

Grid	Three-dimensional	Two-dimensional	% difference
$15 \times 15 \times 11$	7.408	8.105	+9.4%
$21 \times 21 \times 11$	7.021	8.032	+14.4%
$25 \times 15 \times 11$	6.781	7.448	+9.8%

Table 3. Effect of Rayleigh number on an average Nusselt number based on a three-dimensional model: $25 \times 25 \times 11$ grid, $Pr = 0.02$, $A_x = A_z = 1.0$

Ra	10^4	10^5	10^6
$\overline{Nu}$	1.674	3.136	6.781

calculations, and a much more efficient algorithm would be needed.

The effect of aspect ratio A_z on the Nusselt number has been examined to determine the conditions for which the enclosure can be treated as two-dimensional. The results indicate that the spanwise variation of $\overline{Nu}(\zeta)$ increases with the decrease in the aspect ratio. An average Nusselt number (for a grid of $21 \times 21 \times 11$) with aspect ratios of $A_z = 2.0$ and $A_x = 1.0$ is 7.904. This value is close to the value of 8.032 predicted by the two-dimensional model as indicated in Table 2. In this particular example, the two-dimensional model could be used to predict heat transfer with some confidence if aspect ratio A_z is greater than 2. However, for $A_z = 0.5$ and $A_x = 1.0$ an average Nussselt number was found to be 6.740. This, as expected, shows a greater effect of the vertical sidewalls on the circulation in the cavity. The two-dimensional model overpredicts the average Nusselt number by about 16%. In general, the results are consistent in trends with those reported in the literature for ordinary fluids [7], but the percent difference between average Nusselt numbers predicted by two-dimensional model and the three-dimensional model is greater for low Prandtl number fluids.

Past studies have shown that for natural convection flows with $Pr \gtrsim 1$ the role of inertia terms is a minor one. Hence, in theoretical studies $Pr \to \infty$ is a reasonably good approximation for most common fluids. The flows with $Pr \to \infty$ are non-linear solely through advection. The most interesting feature of the results obtained is that the average Nusselt number decreases with Prandtl number. This is consistent in trends with the results for ordinary fluids [7]. Inspection of equation (2) reveals that for fixed Rayleigh number and other parameters, a decrease of Pr is expected to increase axial flow, and would increase the heat transfer rate. However, the velocity distributions (Fig. 6) clearly show that there are multiple longitudinal flows, and that some of these flows are away from the hot end-wall. This explains the reason for the decrease in the average Nusselt number.

Average Nussselt numbers have been calculated using a two-dimensional model for $A_x = 1.0$, and a least-squares fit of the numerical results are represented by an empirical equation

$$\overline{Nu} = 0.16\, Ra^{0.31}\, Pr^{0.14}. \qquad (7)$$

This equation is based on the following range of parameters: $10^4 < Ra < 10^7$ and $0.01 < Pr < 0.05$. Contrary to expectation, the correlation shows that the heat transfer rate would be decreased with the decrease in Prandtl number, but the dependence is quite weak.

Table 4. Average Nussselt number based on two-dimensional model: 41×41 grid, $A_x = 1.0$

	Ra			
Pr	10^4	10^5	10^6	10^7
0.01	1.571	2.975	6.121	13.327
0.02	1.765	3.257	6.701	15.120
0.05	1.978	3.657	7.160	16.936

The above correlation may overpredict heat transfer by about 10% compared to a three-dimensional model. The trends in the results are consistent with those reported for ordinary fluids [7] which have shown that the two-dimensional model also overpredicts the average Nusselt number; however, for ordinary fluids the two-dimensional model overpredicted the three-dimensional model results only between 2.5 and 5%. Since the convergence of the three-dimensional model for a low Pr fluid is quite slow, its use is too costly for parametric studies. Results for the average Nusselt number using a two-dimensional analysis (41×41 grid) have been calculated as a function of Rayleigh and Prandtl numbers and are presented in Table 4.

4.5. *Comparison of predictions with data*

Experiments and corresponding predictions of flow and heat transfer were made for two aspect ratio cavities with three different temperature differences imposed on the end walls of the cavity; however, for the sake of conciseness only two experiments for the largest Rayleigh numbers studied are discussed in detail.

Figure 11 shows a comparison between the predicted and the measured steady-state temperatures in gallium. The symbols denote the data points and the lines the predictions. Although the agreement between the data and predictions is good, the analysis could not match accurately the data at the center of the test cell ($y/H = 1/2$, $z/H = 1/2$). The experimental data are suspect,

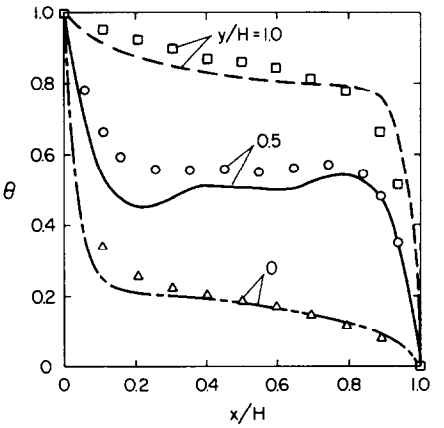

FIG. 11. Comparison of measured and predicted temperature distributions in gallium at $z/H = 1/2$; $Ra = 1.08 \times 10^6$, $Pr = 0.0208$, $A_x = 1.0$, and $A_z = 0.6$.

because at the center of the cavity ($x/H = y/H = z/H = 1/2$) the dimensionless temperature is expected to be 0.5. The discrepancy between the data and predictions could be due to the temperature measurement error, disturbance of flow and temperature field by the thermocouple rake and/or truncation error in the numerical model. Even though the temperature measurement error is estimated to be less than 0.5°C, the results can be significantly affected since the temperature difference between the hot and cold walls is only 14.2°C. Part of the reason for the discrepancy between the measured and predicted temperatures at the top and bottom walls of the enclosure may be due to the fact that the thermocouples embedded in the walls did not measure the true temperature of the fluid but some average temperature of Plexiglass–sealant–gallium system around the junction. Some of the discrepancy between measured and predicted temperatures at the center of the test cell should be attributed to the disturbance of the flow and temperature fields by the thermocouples rate itself, particularly so, because the test cell was relatively small. In addition, since the temperature gradients near the end walls are quite steep the finite-difference grid used may have been too crude.

Temperatures predicted at $y/H = 0.5$ for the conditions of Fig. 11 suggest relatively strong secondary rolls in the cavity to produce axial temperature gradient reversal at $x/H \approx 0.2$ and $x/H \approx 0.8$. The experimental data suggest much weaker circulation, but the axial temperature gradient $\partial\theta/\partial\xi$ is positive in the central region of the cavity. Comparison of experimental data with predictions for the same cavity as for Fig. 11 but a smaller Rayleigh number ($Ra = 2.74 \times 10^5$, $T_H - T_C = 3.6$°C) revealed similar temperature trends and discrepancies. The main difference between the results was that there was practically no uniform temperature region in the center of the cavity at $y/H = 0.5$ as indicated in Fig. 11 for $0.4 < x/H < 0.6$. The predicted and measured temperatures in this region increased very gradually from a minimum located at about $x/H = 0.35$ to a maximum located at about $x/H = 0.65$.

Figure 12 presents a comparison between the measured and predicted temperatures for a different aspect ratio enclosure and Rayleigh number. The agreement between the analysis and data is reasonable throughout the cavity; however, there is discrepancy between the data and predictions at the top and the bottom walls of the cavity. The numerical model predicts steeper temperature gradients than the data near the vertical end walls. This disagreement may in part be due to heat losses to the ambient environment and the physical property variation with temperature since the temperature difference is larger ($T_H - T_C = 34.6$°C).

Comparisons between predicted and measured temperatures have been made for the same cavity as in Fig. 12 having a smaller Rayleigh number ($Ra = 2.35 \times 10^5$, $T_H - T_C = 9.0$°C, not shown here for the sake of conciseness). The temperature discrepancies

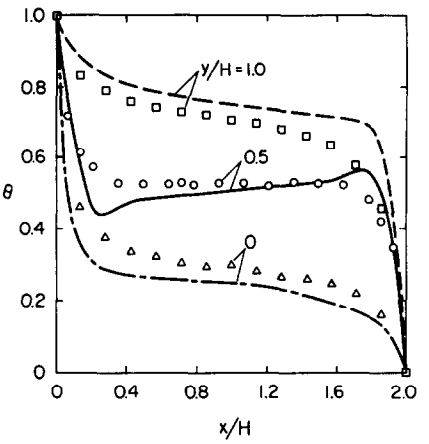

FIG. 12. Comparison of measured and predicted temperature distributions in gallium at $z/H = 1/2$: $Ra = 9.02 \times 10^5$, $Pr = 0.0208$, $A_x = 2.0$, and $A_z = 1.43$.

and trends were similar to those shown in Fig. 12. The predicted local temperature minimum at $x/H = 0.4$ and maximum at $x/H = 0.6$ were not as strong as those shown in Fig. 12, and the temperature between these points increased rather gradually. In this region the predicted temperatures were about 5% smaller than the measured temperatures. This suggests that for $Ra = 2.35 \times 10^5$ the secondary rolls in the center of the cavity are not as intense as for the higher Rayleigh number ($Ra = 9.02 \times 10^5$).

5. CONCLUSIONS

The numerical solutions for flow and temperature fields have been obtained for three-dimensional natural convection as a result of differential end-wall heating. The results show that for low-Prandtl-number fluids three-dimensional effects develop not only near the walls but also in the center of the cavity. Multiple longitudinal flows were shown to develop which are functions of Ra, Pr and the cavity aspect ratios. The numerical results obtained should be considered preliminary. A much finer finite-difference mesh than was used is needed to predict the detailed flow structure with confidence for low-Prandtl-number fluids. For such a purpose, a much more effective algorithm and/or parallel processing would be required to make three-dimensional calculations practical.

The study demonstrates three-dimensional effects on the convective heat transfer throughout the cavity. However, the average Nusselt numbers calculated from a two-dimensional analysis may be used as a first approximation to predict heat transfer in a three-dimensional cavity for low-Prandtl-number fluids and the specific aspect ratios studied.

The experimental temperature data are only in fair agreement with the predictions. Significant studies remain to be done, such as more detailed measurement of the temperature distribution, local and average heat

transfer, and measurement of the velocity field within the enclosure filled with a liquid metal.

Acknowledgements—The work described in this paper was initiated when one of the authors (R. Viskanta) held a Senior U.S. Research Award from the Alexander von Humboldt Foundation. He also gratefully acknowledges the hospitality extended to him by the Technical University of Munich during his study in the Federal Republic of Germany during summer 1984. The authors are indebted to Mr T. H. Song for his assistance with the numerical computations. The computer facilities were made available by Purdue University Computer Center.

REFERENCES

1. I. Catton, Natural convection in enclosures, *Heat Transfer—1978*, Vol. 6, pp. 13–31. Hemisphere, Washington, DC (1978).
2. S. Ostrach, Natural convection in enclosures. In *Advances in Heat Transfer*, Vol. 8, pp. 161–227. Academic Press, New York (1981).
3. S. Ostrach, Natural convection heat transfer in cavities and cells. In *Heat Transfer—1982*, Vol. 1, pp. 365–379. Hemisphere, Washington, DC (1982).
4. I. Catton, A. Bejan, R. Greif and K. G. T. Hollands, Natural convection in enclosures, *Proc. Workshop on Natural Convection*, edited by K. T. Yang and J. R. Lloyd, pp. 24–35, University of Notre Dame, Notre Dame, IN (1983).
5. S. W. Churchill, Free convection in layers and enclosures. *Heat Exchanger Design Handbook*, edited by E. U. Schlunder *et al.*, Chap. 2.5.8. Hemisphere, Washington, DC (1983).
6. H. Ozoe, K. Yamamoto, S. W. Churchill and H. Sayama, Three-dimensional numerical analysis of laminar natural convection in a confined fluid heated from below, *Trans. Am. Soc. mech. Engrs*, Series C, *J. Heat Transfer* **98**, 202–207 (1976).
7. G. D. Mallinson and G. de Vahl Davis, Three-dimensional convection in a box: a numerical study, *J. Fluid Mech.* **83**, 1–31 (1977).
8. A. M. C.-Chan and S. Banerjee, Three-dimensional numerical analysis of transient natural convection in rectangular enclosures, *Trans. Am. Soc. mech. Engrs*, Series C, *J. Heat Transfer* **101**, 114–119 (1979).
9. H. Oertel, Three-dimensional convection within rectangular boxes. In *Natural Convection in Enclosures*, edited by K. E. Torrance and I. Catton, pp. 11–16. ASME, New York (1980).
10. P. K.-B. Chao, H. Ozoe, S. W. Churchill and N. Lior, Laminar natural convection in an inclined rectangular box with the lower surface half-heated and half-insulated, *Trans. Am. Soc. mech. Engrs*, Series C, *J. Heat Transfer* **105**, 425–432 (1983).
11. G. D. Raithby and G. E. Schneider, Numerical solution of problems in incompressible fluid flow: treatment of the velocity–pressure coupling, *Numer. Heat Transfer* **2**, 417–440 (1979).
12. S. V. Patankar, *Numerical Heat Transfer and Fluid Flow*. McGraw-Hill, New York (1980).
13. S. V. Patankar, A calculation procedure for two-dimensional elliptic situations, *Numer. Heat Transfer* **4**, 409–425 (1981).
14. W. H. Cubberly, *Metal Handbook Properties and Selection: Nonferrous Alloys and Pure Metals*, 9th edn, pp. 736–737. American Society of Metals, Metals Park, OH (1979).
15. P. G. Simpkins and T. D. Dudderer, Convection in rectangular cavities with differentially heated endwalls, *J. Fluid Mech.* **110**, 433–456 (1981).
16. G. de Vahl Davis, Natural convection of air in a square cavity: a bench mark numerical solution, *Int. J. numer. Methods Fluids* **3**, 249–264 (1983).

CONVECTION THERMIQUE NATURELLE TRIDIMENSIONNELLE D'UN METAL LIQUIDE DANS UNE CAVITE

Résumé—On décrit un algorithme numérique pour la solution des équations permanentes de Navier–Stokes dans un problème tridimensionnel de convection naturelle dans une cavité rectangulaire avec deux cotés chauffés différemment. Les résultats numériques pour les modèles bi- et tridimensionnel sont fournis pour un fluide à faible nombre de Prandtl dans la cavité. Des expériences utilisant le gallium comme fluide de travail sont décrites. Des températures mesurées sont comparées avec les prévisions du modèle tridimensionnel. L'accord entre les données et le calcul est seulement prometteur et les raisons de l'écart sont identifiées.

DREIDIMENSIONALE WÄRMEÜBERTRAGUNG BEI NATÜRLICHER KONVEKTION EINES FLÜSSIGEN METALLS IN EINEM HOHLRAUM

Zusammenfassung—Die Arbeit beschreibt einen numerischen Algorithmus zur Lösung der dreidimensionalen stationären Navier–Stokes-Gleichungen des Problems der natürlichen Konvektion in einem rechteckigen Hohlraum bei unterschiedlicher Beheizung der Seitenwände. Rechenergebnisse werden für zwei- und dreidimensionale Modelle eines Raumes vorgestellt, der mit einer Flüssigkeit von kleiner *Pr*-Zahl gefüllt ist. Begleitende Versuche mit Gallium als Arbeitsfluid werden beschrieben. Die gemessenen Temperaturen wurden mit Vorausberechnungen des dreidimensionalen Modells verglichen. Die Übereinstimmung zwischen Versuchsdaten und Vorausberechnungen ist nur befriedigend, Gründe für die Abweichung werden angegeben.

ПРОСТРАНСТВЕННАЯ ЕСТЕСТВЕННАЯ КОНВЕКЦИЯ В ЖИДКОМ МЕТАЛЛЕ В ПОЛОСТИ

Аннотация—Описывается алгоритм решения трехмерных стационарных уравнений Навье–Стокса при естественной конвекции в прямоугольной полости при нагреве сбоку. Представлены численные результаты для двух-и трехмерных моделей конвекции в полости, заполненной жидкостью при малых числах Прандтля. Описываются эксперименты, в которых в качестве рабочей жидкости используется галлий. Измеренные температуры сравниваются с расчетами по трехмерной модели. Найдено, что согласие между экспериментальными и расчетными данными является посредственным, и анализируются причины этого расхождения.